

# A phase diagram of the pinch-off-type behavior of impulsively-induced viscoelastic liquid jets

Asuka Hosokawa<sup>1</sup>, Kyota Kamamoto<sup>1</sup>, Hiroya Watanabe<sup>1</sup>, Hiroaki Kusuno<sup>1</sup>, Kazuya U. Kobayashi<sup>2</sup>, Yoshiyuki Tagawa<sup>1\*</sup>

<sup>1\*</sup>Department of Mechanical Systems Engineering, Graduate School of Engineering, Tokyo University of Agriculture and Technology, 2-24-16 Naka-cho, Koganei, 184-8588, Tokyo, Japan.

<sup>2</sup> Department of Mechanical Engineering, Nippon Institute of Technology, 4-1 Gakuendai, Miyashiro-machi, Minamisaitama-gun, 345-8501, Saitama, Japan.

\*Corresponding author(s). E-mail(s): [tagawayo@cc.tuat.ac.jp](mailto:tagawayo@cc.tuat.ac.jp);

## Abstract

In this study, we systematically investigate the jet behaviors of viscoelastic liquids, focusing on the region of high velocity and high viscoelasticity, which has not been investigated in previous studies. We generate viscoelastic jets using an impulsive force and categorize the resulting jets into two types: pinch-off jets (jets that break up during elongation after ejection) and no-pinch-off jets (jets that pull back to the nozzle after maximum elongation or jets that return without elongation after ejection). We then propose criteria to characterize these regions using the Weissenberg number and the Reynolds number, which are dimensionless numbers composed of the rheological properties of the solution and the initial conditions of the jet injection. It is found that pinch-off jets occur at  $Re \gtrsim 23.4Wi$  in regions of high elasticity  $Wi \gtrsim 10$ , and at  $Re \gtrsim 250$  in regions of low elasticity  $Wi \lesssim 10$ . We also show that the phase diagram can be explained by modeling a focused jet using the finitely extensible non-linear elastic dumbbell model with the Chilcott–Rallison closure approximation (FENE-CR).

**Keywords:** Viscoelasticity, Liquid jet, Jet Breakup, FENE dumbbell fluids

# 1 Introduction

Liquid jets have been studied in the past from a variety of perspectives due to their significance in fundamental research and their widespread occurrence (Eggers and Villermaux, 2008). Practical applications of liquid jets have also been demonstrated in inkjet printing (Derby, 2010), pharmaceutical sprays (Villermaux et al., 2004), and agricultural irrigation (Kincaid et al., 1996).

In order to develop these applications, there is a need to elucidate the breakup process of liquid jets. Previous studies have shown that the addition of polymers to liquid jets can significantly change this process (Clasen et al., 2006). In particular, in inkjet printing, the addition of polymers has a significant effect on the splitting of liquid filaments generated from the nozzle (Bazilevskii et al., 2005). The addition of small amounts of high molecular weight polymers can inhibit the formation of undesirable satellite droplets, thus improving print clarity. On the other hand, a ‘bungee-jumper jet’ is observed when the polymer concentration is high (Morrison and Harlen, 2010). This refers to a phenomenon in which a jet is generated, maximally elongated, and then pulled back to the initial interface due to the elasticity of the liquid. Such a jet interferes with the detachment of droplets produced by the nozzle and with the coating of the liquid. Therefore, various studies have been conducted to clarify and control the bungee-jumper jet phenomenon using numerical simulations (Morrison and Harlen, 2010; Torres and Fonte, 2022) and experiments (Turkoz et al., 2018; Bazilevskii et al., 2005).

However, these studies have been limited to the injection of low-velocity ( $< O(10^0)$  m/s) and low-viscosity ( $< 20$  mPa·s) solutions used in conventional inkjet printing (Franco-Gómez et al., 2021). In recent years, next-generation printing technologies such as 3D printing (Truby and Lewis, 2016) and artificial cell printing (Noor et al., 2019) have been developed. Viscoelastic liquids are among the non-Newtonian fluids used in these printing techniques, and there is a need to understand the behavior of jets with a wide range of viscoelastic properties to further develop next-generation printing technologies. Therefore, it is essential to investigate jet behavior at high velocities ( $\geq O(10^1)$  m/s) and in the highly viscoelastic regime ( $De > O(10^1)$ ). Here,  $De$  is the Deborah number, a dimensionless number that indicates the ratio of the elastic and inertia-capillary time scales.

One technique for producing high-velocity jets is the focused liquid jet injection technique (Tagawa et al., 2012; Peters et al., 2013). A focused jet is a jet in which the jet tip diameter is smaller than the jet bottom diameter (Gordillo et al., 2020). A well-known example is the Worthington jet, which is generated when a solid sphere or droplet impacts the surface of a liquid bath (Worthington, 1908). Antkowiak et al. (2007) developed a method to generate focused liquid jets by having a liquid-filled container free fall and collide with the floor, providing a rapid acceleration at the concave gas-liquid interface. This method can generate a focused jet easily and is highly controllable (Kiyama et al., 2016). Onuki et al. (2018) developed a method of jet generation by inserting a small tube inside a container. This method can eject a liquid with a viscosity 50 times higher than that from conventional methods (1000 mPa·s).

The aim of this study is to elucidate jet behaviors at high velocity and high viscoelasticity. For this purpose, a high-velocity focused liquid jet is generated using an impulsive force and observed using a high-speed camera. We also use polymers of different molecular weights and concentrations to help the viscoelastic liquids achieve high viscoelasticity. By analyzing the observed jets in detail and classifying them using two dimensionless numbers, we attempt to understand the jet behavior of viscoelastic liquids.

## 2 Focused jet generation

### 2.1 Jet generator using a test tube

A schematic diagram of the experimental setup is shown in Fig. 1. A test tube (A-16.5, Maruemu, inner diameter  $2r = 14.3$  mm) is filled with liquid (liquid height  $L = 32$  mm) and suspended by an electromagnet. When the electromagnet is switched off, the test tube falls freely. During this time, the gas-liquid interface inside the test tube develops a concave shape due to the capillary force. When the test tube collides with the floor, the liquid is accelerated over a very short time, and as a result, a focused liquid jet is formed from the gas-liquid interface (Kiyama et al., 2016).

In this experiment, the initial velocity  $U_0$  of the fluid is controlled by varying the drop height of the test tube ( $H = 3\text{--}300$  mm) and the floor material (SS400, nitrile rubber). The initial velocity  $U_0$  is the sum of the impact velocity  $V_0$  of the test tube to the floor and the bounce velocity  $V'$  of the test tube from the floor, expressed as in Eq. 1 (Kiyama et al., 2014). In this case, the impact velocity  $V_0$  of the test tube on the floor is given by Eq. 2, which is derived from the energy conservation law, where  $g$  is the gravitational acceleration. The bounce velocity  $V'$  of the test tube is given by Eq. 3, where  $H'$  is the bounce velocity of the test tube 10 ms after impact ( $t = 0$  ms).

$$U_0 = V_0 + V'. \quad (1)$$

$$V_0 = \sqrt{2gH}. \quad (2)$$

$$V' = \frac{H'}{t}. \quad (3)$$

The jet formation is captured using a high-speed camera (FASTCAM SA-X, Photron) and a backlight (White Led Backlight, Phlox) at 30,000 fps.

### 2.2 Jet generator using a double-layer narrow tube

We use an injection device with a capillary tube to generate jets using the impulsive force (Onuki et al., 2018). A schematic diagram of the experimental setup is shown in Fig. 2. In this experiment, a glass capillary tube (Fuji Science Industry, inner diameter  $2r = 2$  mm) is inserted into a container partially filled with liquid and sealed outside the tube. We control the pressure of the sealed air outside the tube using a syringe in order to push the liquid interface inside the capillary near to the bottom of the container and thus change the position of the liquid surface inside the capillary

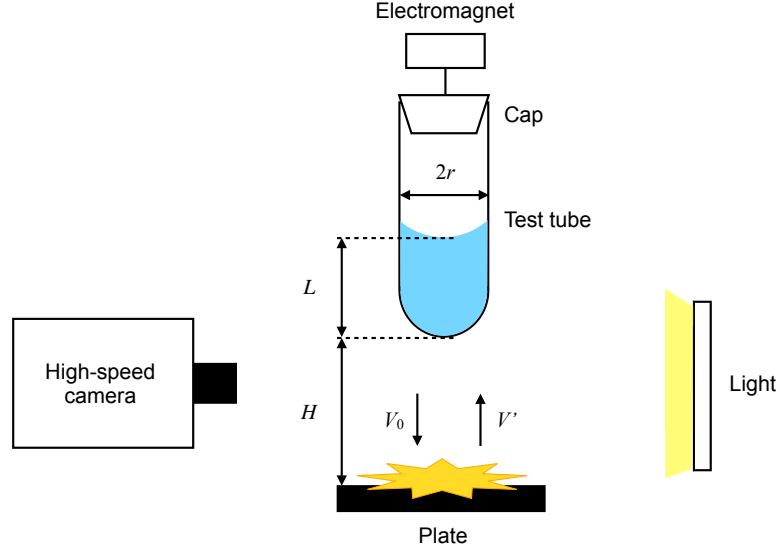


**Fig. 1** The experimental setup for generating a focused jet using a falling test tube

$L_{cap}$ . The liquid level inside the tube is kept deeper than that outside the tube. An electromechanical device (ShinDengen solenoids, KGK power supply) is used to apply a vertical upward impulsive force at a velocity  $V_0$ . The liquid inside the tube is rapidly accelerated and a focused jet is generated from the inside of the tube. The initial velocity  $U_0$  of the generated jet varies depending on the ratio of the distance between the gas-liquid interface outside the tube  $L_{top}$  and the liquid surface position inside the tube  $L_{cap}$ . The initial velocity  $U_0$  is calculated using the following equation (Onuki et al., 2018):

$$U_0 = \frac{L_{top}}{L_{cap}} V_0. \quad (4)$$

The jet formation is captured using a high-speed camera and a backlight at 30,000–60,000 fps.

### 3 Properties of the liquid solutions

Polymer solutions were used as the viscoelastic liquids in the experiments (Table 1). We used two types of polymers: polyethylene oxide (Sigma-Aldrich, molecular weight  $M_w = 0.4, 2, 5,$  and  $8$  M (= million), polymer concentration  $c = 0.5, 1,$  and  $2$  wt%) and polyacrylamide (Sigma-Aldrich,  $M_w = 5\text{--}6$  M,  $c = 0.2, 0.4,$  and  $0.8$  wt%). The solutions were prepared by adding polyethylene oxide (PEO) and polyacrylamide (PAM) to pure water and aqueous-glycerin solution (glycerol: 70 wt%, water: 30 wt%, G70W30) as solvents and stirring at 650 rpm, 60 °C for 24 to 48 hours.

Polymer solutions generally exhibit shear-thinning behavior, in which the viscosity decreases with an increasing strain rate. The shear viscosities of the PEO and PAM

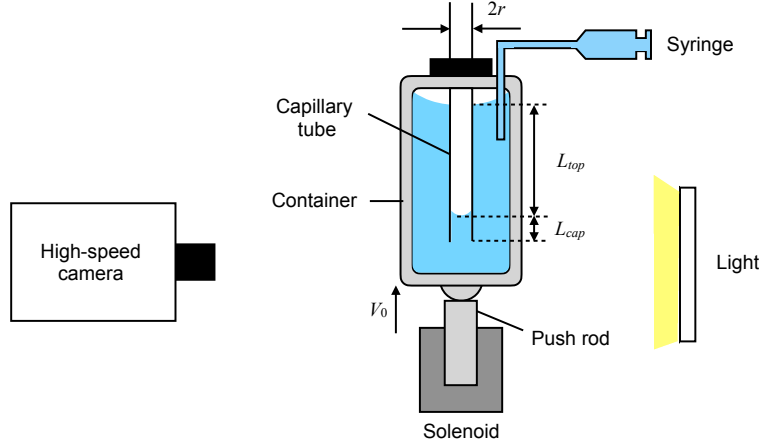


**Fig. 2** The experimental setup for generating a focused jet using the impact-induced jet generator. The capillary tube is inserted into the liquid, with the liquid level inside the tube set deeper than that outside the tube

solutions as measured with a shear rheometer (MCR-302, Anton Paar) are shown in Fig. 3. The dashed line in Fig. 3 represents the confidence limit of the measured shear viscosity due to the torque sensitivity of the shear rheometer (Gaillard et al., 2019). From Fig. 3, the shear viscosity  $\mu_s$  of both the PEO and PAM solutions decreases with an increasing shear rate  $\dot{\gamma}$ , indicating shear-thinning properties. In both solutions, the higher the molecular weight and concentration, the greater the shear viscosity and the greater the slope of the shear curve. The higher the molecular weight and concentration, the greater the viscoelasticity and thus, the stronger the shear-thinning property (Dinic et al., 2017).

Viscoelastic liquids also have spring-like elastic properties. We use the relaxation time  $\lambda$  as a physical property value to express the magnitude of the elasticity.  $\lambda$  is calculated using dripping-onto-substrate capillary breakup elongation rheometry

**Table 1** The physical properties of the solutions

	Solutions	Density $\rho$ [kg/m <sup>3</sup> ]	Surface tension $\sigma$ [mN/m]	Relaxation time $\lambda$ [ms]
PEO	0.4M 1wt%	999.7	64.0	1.9
	2M 1wt%	998.3	64.1	12.4
	5M 0.5wt%	996.4	62.8	35.4
	5M 1wt%	998.0	62.0	57.2
	8M 1wt%	981.4	60.6	207.6
	8M 2wt%	999.1	62.1	301.4
PAM	5-6M 0.2wt%	995.2	72.5	3.3
	5-6M 0.4wt%	1002.8	63.0	4.6
	5-6M 0.8wt%	1000.0	71.0	16.5
	5-6M 0.4wt% (G70W30)	1176.9	66.4	91.0

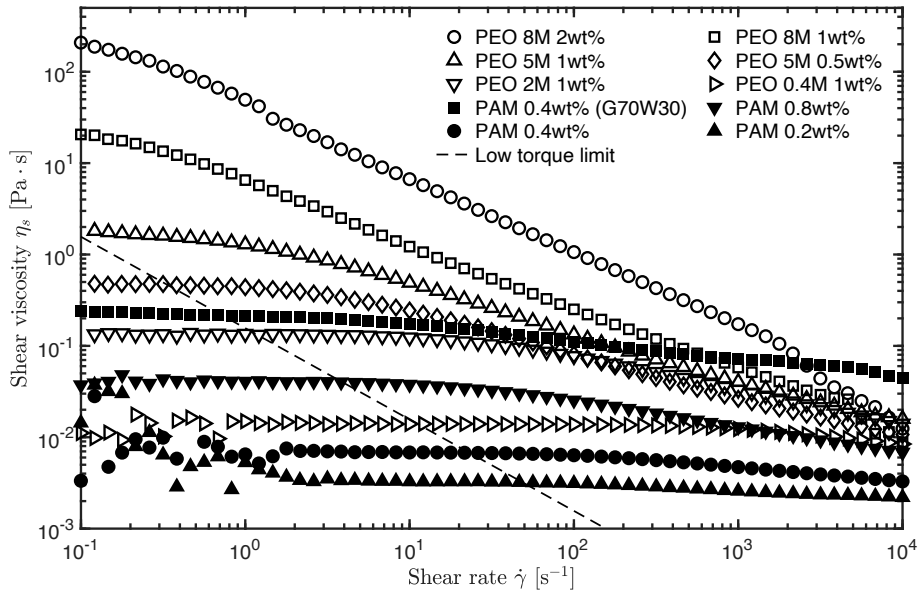


**Fig. 3** The shear viscosity for the PEO and PAM solutions

(DoS-CaBER), which is a method for evaluating the extensional rheology of viscoelastic liquids. This method enables the measurement of the relaxation times of low-viscoelastic liquids, which are difficult to measure with rheometers (Dinic et al., 2015; Sur and Rothstein, 2018). Figure 4 shows the experimental DoS-CaBER setup. First, the sample is pushed out of a syringe to form a droplet at the tip of the nozzle (outer diameter  $2R_0 = 1.27$  mm, inner diameter  $2R_i = 0.97$  mm). When the droplet adheres to the glass plate with its own weight, the liquid spreads on the glass plate and forms a liquid thread due to the surface tension. The liquid thread becomes thin and shreds gradually. The force that resists the surface tension acting on the liquid thread differs depending on the solution, and the elastic force is dominant in viscoelastic liquids (in the elasto-capillary regime) (Anna and McKinley, 2001). The time evolution equation of the liquid thread radius  $R$  formed in this case is expressed as (Mathues et al., 2018):

$$\frac{R(t)}{R_0} \propto \exp\left(-\frac{t}{3\lambda}\right), \quad (5)$$

where  $R_0$  is the nozzle radius and  $t$  is the time since the liquid thread was formed. Therefore, the relaxation time  $\lambda$  of the sample can be calculated from the time evolution of the liquid thread radius  $R$ .

An example analysis of the liquid relaxation time  $\lambda$  using DoS-CaBER is shown in Fig. 5. The horizontal axis is the time  $t$  and the vertical axis is the dimensionless liquid thread radius  $R/R_0$ , which is the liquid thread radius  $R$  divided by the nozzle radius  $R_0$ . The plot shows a 5M 1wt% PEO solution. Since the elongation rate is constant

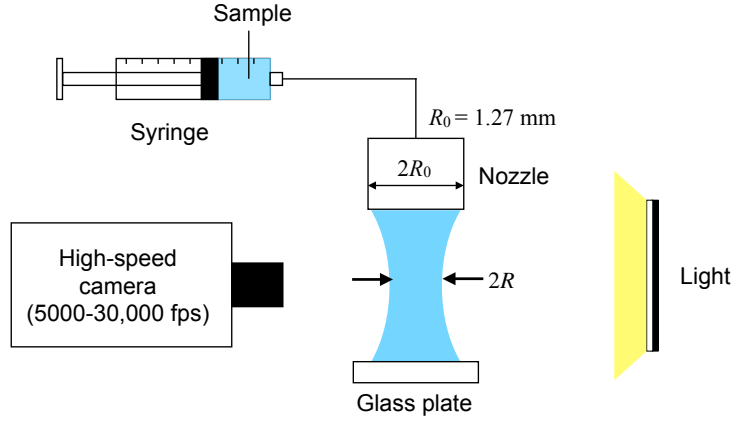


**Fig. 4** The experimental setup for the dripping-onto-substrate capillary breakup extensional rheometry: DoS-CaBER

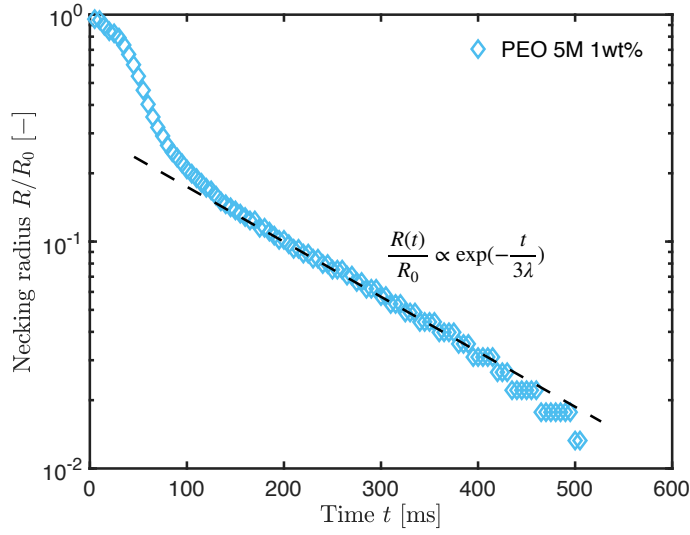


**Fig. 5** The non-dimensional radius (the ratio of the neck radius to the nozzle radius) as a function of time for 5M 1wt% PEO shown on a semi-log plot. The dashed lines show the fitted region obtained using Eq. 5

in the elasto-capillary regime, the elongation rate is calculated from the DoS-CaBER experimental results and the elasto-capillary regime is determined. An exponential approximation is made in this region, and the relaxation time  $\lambda$  is derived using Eq. 5.

The relaxation times  $\lambda$  for the PEO and PAM solutions are calculated using the same procedure and the results are shown in Table 1. The relaxation time  $\lambda$  increases with an increasing concentration  $c$  and molecular weight  $M_w$  for both the PEO and

PAM solutions. In a previous study, it was reported that the relaxation time  $\lambda$  increases with increasing polymer concentration  $c$  and molecular weight  $M_w$ , and we believe that this result is consistent (Dinic et al., 2017). In addition, when comparing 2M 1wt% and 5M 0.5wt% PEO solutions,  $\lambda$  is larger for 5M 0.5wt%. This is because the molecular weight  $M_w$  makes a larger contribution to the relaxation time  $\lambda$  than the concentration  $c$  (Bazilevskii et al., 2005).

## 4 Results and Discussions

In this experiment, we have succeeded in identifying two different types of jets through systematic experiments by varying the magnitude of the viscoelasticity and initial velocity.

The typical behaviors of the generated viscoelastic liquid jets are shown in Fig. 6. Note that the  $t = 0$  ms time of the test tube impacting the floor is used as the reference time, and the time evolution from that point is shown in Fig. 6. Figure 6(a) shows images of a jet generated by the ejection of a 0.4M 1wt% PEO solution at an initial velocity of  $U_0 = 0.84$  m/s. The jet ejected from the interface has a shape in which the tip diameter is smaller than the tail diameter, indicating that it is a focused jet. After ejection, the focused jet is elongated vertically upward, and the tip is pinched off at  $t = 63$  ms. Thus, we define this type of jet as a ‘pinch-off jet’. Figure 6(b) shows images of a jet generated by ejecting an 5M 1 wt% PEO solution at an initial velocity of  $U_0 = 2.9$  m/s. The jet is elongated after ejection from the interface and reaches its maximum length at  $t = 23$  ms. After that, the jet returns to the initial interface. It should be noted that the jet is prevented from being pinched off despite the large impact force applied in Fig. 6(b) compared to that in Fig. 6(a). This phenomenon was also observed in a previous study as a ‘bungee-jumper jet’ when the elasticity of the solution is large (Franco-Gómez et al., 2021), and it is believed that the elastic force contributes to the pulling back of the jet. We define such a jet that pulls back to the initial interface after maximum elongation as a ‘no-pinch-off jet’. Finally, Fig. 6(c) shows images of a jet generated by ejecting a 8M 1 wt% PEO solution at an initial velocity of  $U_0 = 1.2$  m/s. The jet is ejected from the interface but returns to the initial interface without elongation. The reason for this is presumed to be that the initial velocity is smaller in Fig. 6(c) than in Fig. 6(b), i.e., the jet is not given a sufficient impulsive force to generate a jet. Such jets are also defined as ‘no-pinch-off jets’.

These changes in jet behavior are considered to be caused by the balance between the viscoelasticity of the liquid and the inertial force that dominates during jet extension. We organize our results in terms of two dimensionless numbers. One is the Weissenberg number  $Wi$ , which represents the ratio of the elastic force to the viscous force, and is defined as

$$Wi = \frac{\lambda U_0}{r}. \quad (6)$$

The other is the Reynolds number  $Re$ , which represents the ratio of the inertial force to the viscous force, and is defined as

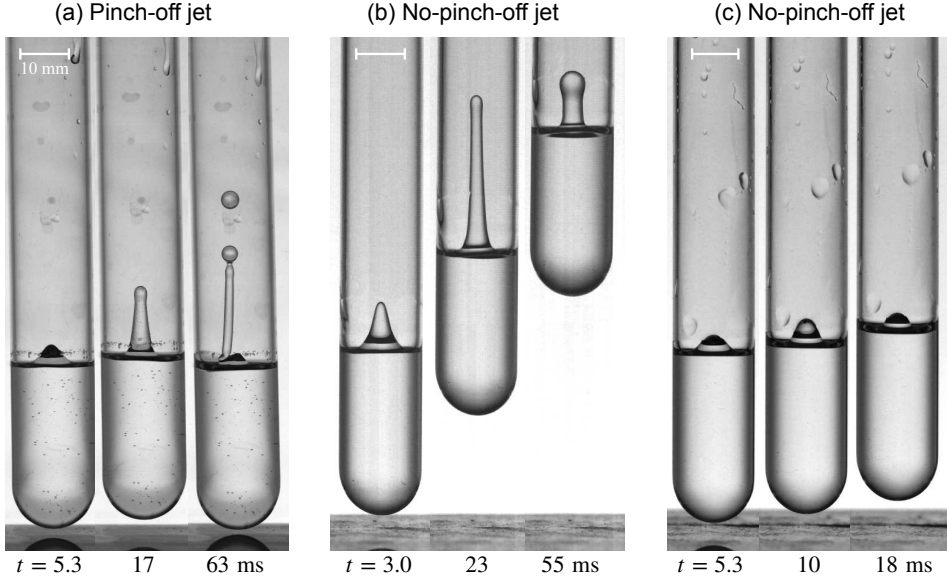


**Fig. 6** Viscoelastic liquid jets can be divided into two typical types: (a) pinch-off jets and (b)(c) no-pinch-off jets. (a) Images of a jet generated by the ejection of a 0.4M 1wt% PEO solution at an initial velocity of  $U_0 = 0.84$  m/s. The jet is ejected from the interface and extends vertically upward, and the tip is pinched off after a certain time. (b) Images of a jet generated by the ejection of an 5M 1wt% PEO solution at an initial velocity of  $U_0 = 2.9$  m/s. The jet is elongated after ejection from the interface and, after maximum elongation, pulled back to the initial interface. (c) Images of a jet generated by the ejection of a 8M 1wt% PEO solution at an initial velocity of  $U_0 = 1.2$  m/s. The jet is ejected from the interface but returns to the initial interface without elongation

$$Re = \frac{\rho U_0 r}{\mu_s}, \quad (7)$$

where  $\rho$  is the density of the solution. Since the polymer solution used in this experiment has shear-thinning properties, we calculate the strain rate  $\dot{\gamma}$  from the elongation behavior of the jet ( $\dot{\gamma} = O(10^2-10^3)$ ) and assume the shear viscosity  $\mu_s$  at that strain rate as the representative viscosity.

The results of organizing the jet behaviors using the Weissenberg number  $Wi$  and the Reynolds number  $Re$  are shown in Fig. 7. The error bars in Fig. 7 indicate the error range associated with the estimation of the shear viscosity  $\mu_s$ . The higher the viscoelasticity of the liquid, the greater the shear-thinning property, resulting in a larger error in the region of high  $Wi$ .

Figure 7 shows that the jet behavior can be divided into two regions, pinch-off and no-pinch-off jets, depending on  $Wi$  and  $Re$ . The fact that the results can be organized by parameters related to the physical properties of the solution and the initial conditions of jet injection suggests that these parameters have a significant effect on the behavior of the viscoelastic liquid jets. Furthermore, the experimental results are well-organized in a unified manner regardless of the type of polymer (PEO or PAM). Therefore, the effect of the type of polymer on the jet behavior is considered

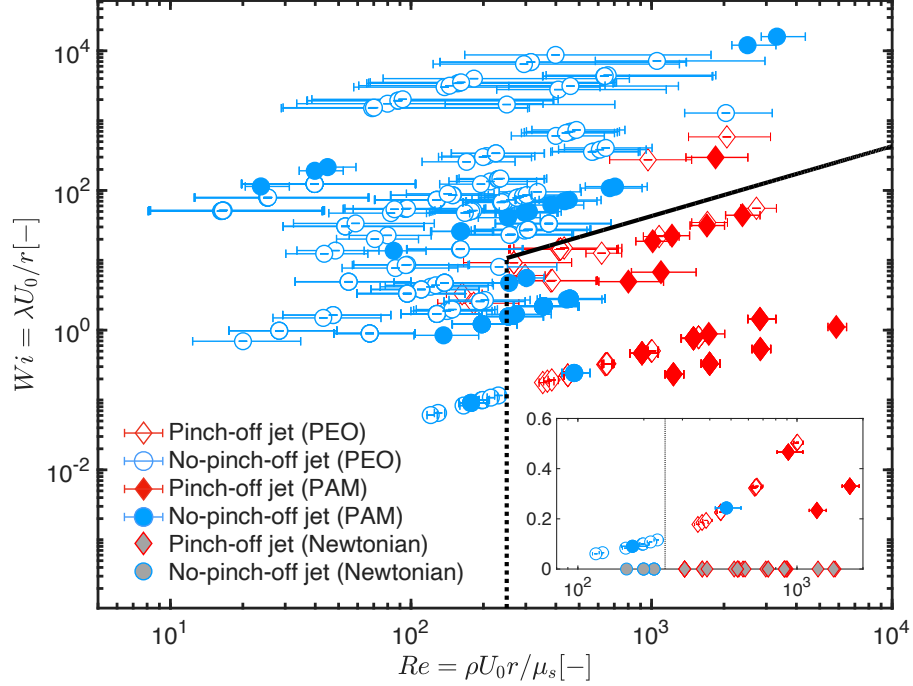


**Fig. 7** A phase diagram of the impulsively-induced jet behavior of viscoelastic liquids with a Weissenberg number  $Wi$  and Reynolds number  $Re$ . The outer frame of the plot indicates the jet type: red indicates a pinch-off jet and blue indicates a no-pinch-off jet. The markers in the plot indicate the type of solution: a lack of markers indicates PEO solutions, markers indicate PAM solutions, and gray markers indicate an aqueous-glycerin solution, which is a Newtonian fluid. The inner figure shows the region with low  $Wi$  ( $Wi \leq 0.6$ ) in detail

to be small in this study. In the following, we will discuss the jet behavior in detail in two regions: 1) the region with  $Wi \gtrsim 10$  and 2) the region with  $Wi \lesssim 10$ .

#### 4.1 The region with $Wi \gtrsim 10$

Figure 7 shows that in the region with  $Wi \gtrsim 10$ , a no-pinch-off jet occurs in the region with high  $Wi$  and a pinch-off jet occurs in the region with low  $Wi$ . It should be noted that even for a sufficiently high  $Re$ ,  $Re \gtrsim O(10^3)$ , the pinching off of the jet is inhibited in the region with high  $Wi$  ( $Wi \gtrsim O(10^3)$ ). Since the elasticity increases with increasing  $Wi$ , this phenomenon is considered to be caused by the elasticity of the viscoelastic liquids.

To understand this phenomenon, we model a jet using a viscoelastic model following previous studies (McIlroy et al., 2013; Hoath et al., 2012). The effect of elasticity on the jet behavior can be evaluated by introducing a constitutive equation that accounts for elastic stress (Turkoz et al., 2021). There are various models, but here we use the

finitely extensible non-linear elastic dumbbell model with the Chilcott–Rallison closure approximation, known as the FENE-CR model (Chilcott and Rallison, 1988). The FENE-CR model is one of the simple constitutive equations used for the rheological properties of polymer solutions.

Assuming an incompressible fluid, the continuity equation and Navier–Stokes equation can be expressed using the fluid velocity  $\mathbf{u}$ , pressure  $p$ , and stress tensor  $\boldsymbol{\sigma}$  as

$$\nabla \cdot \mathbf{u} = 0, \quad (8)$$

$$\rho \frac{D\mathbf{u}}{Dt} = -\nabla p + \nabla \boldsymbol{\sigma}. \quad (9)$$

In the FENE-CR model, the stress is given by

$$\boldsymbol{\sigma} = 2\mu_s \mathbf{E} + Gf(\mathbf{A} - \mathbf{I}), \quad (10)$$

$$\frac{D\mathbf{A}}{Dt} = \nabla \mathbf{u} \cdot \mathbf{A} + \mathbf{A} \cdot (\nabla \mathbf{u})^T - \frac{f}{\lambda}(\mathbf{A} - \mathbf{I}), \quad (11)$$

where  $\mathbf{E} = (\nabla \mathbf{u} + \nabla \mathbf{u}^T)/2$  is the strain rate tensor,  $\mathbf{G}$  is the elastic modulus,  $\mathbf{I}$  is the unit matrix,  $\mathbf{A}$  is the conformation tensor related to the deformation of the polymer chains, and  $f$  is a nonlinear function that enforces finite extensibility. Using the elongation limit of the polymer chain  $L$ ,  $f$  is expressed as

$$f = (L^2 - \text{tr}(\mathbf{A})/L^2)^{-1}. \quad (12)$$

Since the tip of the jet is faster than the tail, we assume that the inertia at the tip of the jet affects the jet behavior, and propose a simple model as shown in Fig. 8. We define the initial condition to be  $t = t_r$ , which is the time when the jet tip is ejected by a distance  $r$  (=representative length) from the initial interface in Fig. 8(a). The jet velocity at this time is  $U_r$ . The jet then decelerates to a velocity  $U$ , and the jet tail deforms uniformly with time from an initial length  $r$  and then increases to  $z$  at time  $t$  (Fig. 8(b)). The volume of fluid at the tip  $\Omega_{tip}$  and at the tail  $\Omega_{tail}$  are assumed constant.

When viscous and elastic forces act on the jet, the equation of motion of the tip is given by

$$\rho \Omega_{tip} \frac{dU}{dt} = -\frac{\Omega_{tail}}{z} \left( \frac{3\mu_s U}{z} + Gf(A_{zz} - A_{rr}) \right). \quad (13)$$

Assuming an axisymmetric flow, Eq. 11 can be expanded into an axial component  $A_{zz}$  and a radial component  $A_{rr}$ , which can be expressed as follows:

$$\frac{dA_{zz}}{dt} = \left( \frac{2U}{z} - \frac{f}{\lambda} \right) A_{zz} + \frac{f}{\lambda}, \quad (14)$$

$$\frac{dA_{rr}}{dt} = -\left( \frac{U}{z} + \frac{f}{\lambda} \right) A_{rr} + \frac{f}{\lambda}. \quad (15)$$

Furthermore, assuming that the axial elongation of the polymer chain is sufficiently large ( $A_{zz} \gg 1$ ,  $A_{zz} \gg A_{rr}$ ), we can write  $A_{zz} \sim (z/r)^2 e^{-t/\lambda}$ . Assuming that the

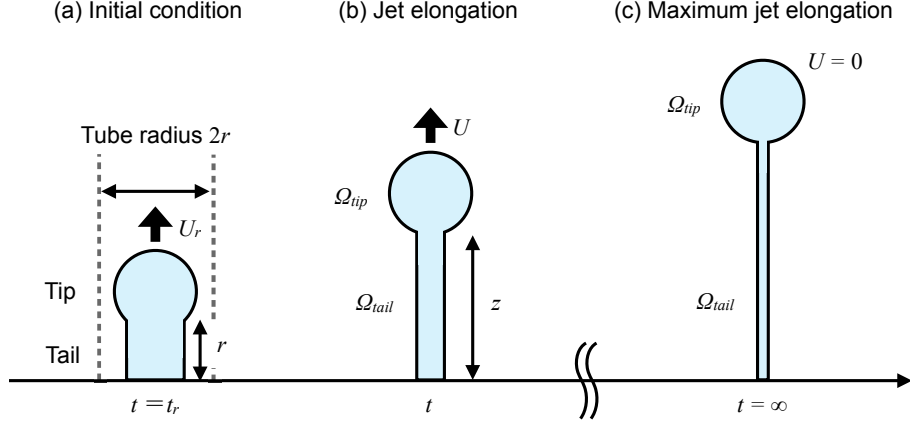


**Fig. 8** A simplified model of the viscoelastic jet

elastic deformation is smaller than the elongation limit ( $A_{zz} \ll L^2 \rightarrow f \sim 1$ ), it can be expressed as  $A_{rr} \sim 0$ . Therefore, the deceleration  $\Delta U$  at position  $z$  ( $z > r$ ) is obtained by integrating Eq. 13 at time  $t$  (Fig. 8(b)).

$$\rho\Omega_{tip}\Delta U(z) = -\Omega_{tail}\left(3\mu_s\left(\frac{1}{r} - \frac{1}{z}\right) + \frac{G}{r^2}\int_r^z ze^{-\frac{z}{\lambda}}dt\right). \quad (16)$$

Assuming  $U = 0$  when  $z \rightarrow \infty$  (Fig. 8(c)),

$$\rho\Omega_{tip}U_r = \Omega_{tail}\left(\frac{3\mu_s}{r} + \frac{U_r}{r^2}G\lambda^2\right). \quad (17)$$

When the elastic term is sufficiently large compared with the viscous term, Eq. 17 can be transformed into

$$\rho\Omega_{tip}U_r = \Omega_{tail}\frac{U_r}{r^2}G\lambda^2. \quad (18)$$

Assuming that the jet tip diameter  $d_{tip}$  and the tail diameter  $d_{tail}$  satisfy  $d_{tip} \sim \alpha r$  and  $d_{tail} \sim r$  in the initial state (Fig. 8(a)), then  $\Omega_{tip} \sim 4\pi(\alpha r/2)^3/3$ ,  $\Omega_{tail} \sim \pi r^3/4$ . Note that  $\alpha$  is a constant. Furthermore, assuming  $G \sim \mu_s\lambda$  and  $U_r \propto U_0$ , and substituting these into Eq. 18, we obtain

$$Re \sim \frac{3}{2\alpha^3}Wi. \quad (19)$$

For  $Re \lesssim 3/(2\alpha^3)Wi$ , the jet is pulled back by the elastic force, resulting in a no-pinch-off jet, and for  $Re \gtrsim 3/(2\alpha^3)Wi$ , a pinch-off jet occurs due to the lack of elastic force. The experimental value of  $\alpha$  is  $\alpha \sim 0.4$ . From the above, it is suggested that the thresholds of the no pinch-off jet and pinch-off jet in Fig. 7 can be expressed by the following equation.

$$Re \sim 23.4Wi. \quad (20)$$

## 4.2 The region with $Wi \lesssim 10$

From Fig. 7, no-pinch-off jets are observed for  $Re \lesssim 250$  and pinch-off jets are observed for  $Re \gtrsim 250$  when  $Wi \lesssim 10$ . This is considered to be because the elasticity of the solution has little effect on the jet behavior in the low  $Re$  region, and the jet behaves like a Newtonian fluid. In a previous study, the effect of viscosity on the jet velocity of a Newtonian fluid was investigated (Onuki et al., 2018). It was reported that a viscous boundary layer develops on the wall surface at  $Re \lesssim 200$ , which prevents the focusing effect of the flow. Therefore, the lower  $Re$  is in the present study, the more the viscous boundary layer develops on the wall surface and near the free surface, which prevents jet extension.

Therefore, in Eq. 17, when the viscous term is sufficiently large compared to the elastic term, the equation can be transformed into

$$\rho\Omega_{tip}U_r = \Omega_{tail}\frac{3\mu_s}{r}. \quad (21)$$

Assuming  $d_{tip} \propto r$  and  $d_{tail} \sim r$  as before,  $\Omega_{tip}$  and  $\Omega_{tail}$  can be calculated and substituted into Eq. 21. Also, assuming  $U_r \propto U_0$ , Eq. 21 can be transformed into

$$Re \sim \beta, \quad (22)$$

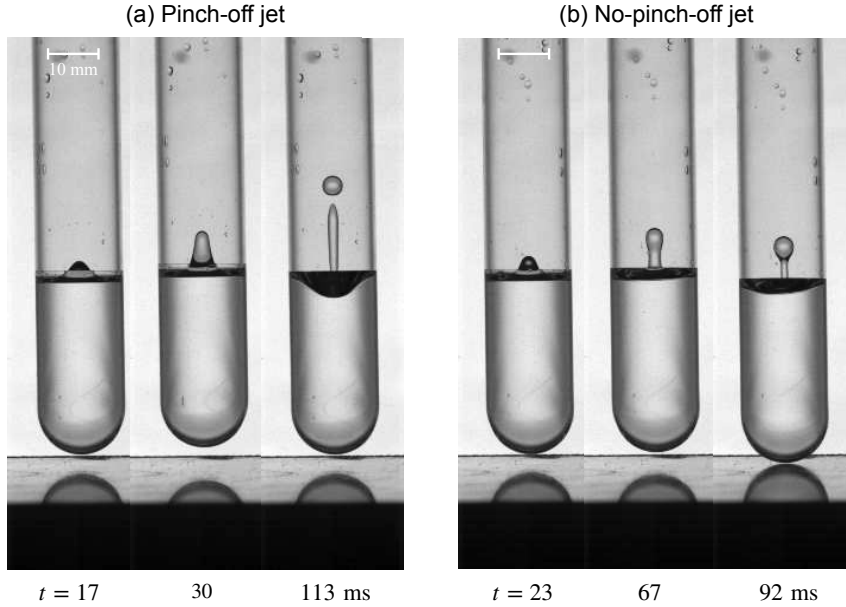


**Fig. 9** The jet behavior of aqueous-glycerin solution (G70W30). (a) A jet ejected from the interface and extended vertically upward, with the tip pinched off after a certain time when  $Re \sim 370$ . (b) A jet ejected from the interface but returned to the initial interface without being pinched off when  $Re \sim 230$

where  $\beta$  is a constant. For  $Re \lesssim \beta$ , a no-pinch-off jet is expected to occur because the viscosity prevents the jet extension, and for  $Re \gtrsim \beta$ , a pinch-off jet is expected to occur because the inertial force is sufficient.

To confirm that the elasticity of the solution does not affect the jet behavior in this region, we investigated the jet behavior of a Newtonian fluid, aqueous-glycerin solution (G70W30) where the density  $\rho$ , viscosity  $\mu_s$ , and surface tension  $\sigma$  of the glycerin solution are  $\rho = 1175.4$  [kg/m<sup>3</sup>],  $\mu_s = 0.0169$  [Pa · s], and  $\sigma = 68.4$  [mN/m], respectively. Here, the range of the surface tension for the viscoelastic liquids and aqueous-glycerin solution used in this experiment is  $\sigma = 62.0\text{--}72.5$  [mN/m]. Therefore, the effects of surface tension (Rayleigh instability) on the jet behavior are considered to be almost equivalent. Figure 9 shows a typical image of a G70W30 jet. As shown in Fig. 9(a), when  $Re \sim 370$ , the jet is pinched off at the tip after extension and a pinch-off jet is generated. On the other hand, when  $Re \sim 230$ , as shown in Fig. 9(b), the jet returns to the initial interface without being pinched off after ejection, so a no-pinch-off jet is generated. We determined from the experiments that the jet behaviors of the Newtonian fluid transitioned from no-pinch-off to pinch-off at  $Re \sim 250$  (Fig. 7). Therefore, in Eq. 22, the  $\beta$  obtained from the experiments is  $\beta \sim 250$ , and the threshold in the region of low  $Wi$  is

$$Re \sim 250. \quad (23)$$

In Fig. 7, the no-pinch-off and pinch-off jets can be generally distinguished using Eq. 20 (solid line) and Eq. 23 (dashed line). Therefore, it is concluded that the jet behavior can be classified through modeling with the FENE-CR model.

## 5 Conclusion

In this study, we have conducted systematic experiments on jet behaviors in the high-viscoelasticity and high-velocity regime, which have not been investigated before. We injected a polymer solution with a wide range of viscoelasticities as a focused jet and observed two characteristic behaviors. These behaviors are: 1) After injection in the vertically upward direction, the jet is elongated and after a certain amount of time, the tip is pinched off (pinch-off jet). 2) After injection, the jet is elongated and after maximum elongation, it is pulled back to the initial interface, or after injection, it returns to the interface without elongation (no-pinch-off jet). It is suggested that these jet behaviors can be predicted using the Weissenberg number  $Wi$  and the Reynolds number  $Re$ , which are dimensionless numbers composed of the rheological properties of the solution and the initial conditions of the jet injection. Furthermore, we modeled this phenomenon using a viscoelastic model, the FENE-CR model, and obtained good agreement with the experimental results.

We believe that this study provides significant insight into the viscoelasticity of jets with a focused geometry. Furthermore, it will be useful for clarifying the effects of viscoelasticity on the breakup processes of various liquid jets.

## Declarations

**Conflict of interest.** The authors declare that they have no conflict of interest.

**Ethics approval.** Not applicable, because this article does not contain any studies with human or animal subjects.

**Informed consent.** Not applicable.

**Funding.** This work was supported by JSPS KAKENHI Grant Number JP20H00223.

**Author Contributions.** AH: investigation, experiments, writing original draft, and editing. KK: discussion of organizing experimental results. HW: discussion of modeling. HK: discussion of modeling. KUK: design of study, supervision, and supporting for original draft. YT: design of study and supervision.

## References

- Eggers, J., Villermaux, E.: Physics of liquid jets. *Rep. Prog. Phys.* **71**(3), 036601 (2008) <https://doi.org/10.1088/0034-4885/71/3/036601>
- Derby, B.: Inkjet Printing of Functional and Structural Materials: Fluid Property Requirements, Feature Stability, and Resolution. *Annu. Rev. Mater. Res.* **40**(1), 395–414 (2010) <https://doi.org/10.1146/annurev-matsci-070909-104502>
- Villermaux, E., Marmottant, P., Duplat, J.: Ligament-Mediated Spray Formation. *Phys. Rev. Lett.* **92**, 074501 (2004) <https://doi.org/10.1103/PhysRevLett.92.074501>
- Kincaid, D.C., Solomon, K.H., Oliphant, J.C.: Drop Size Distributions for Irrigation Sprinklers. *Trans. ASABE* **39**(3), 839–845 (1996) <https://doi.org/10.13031/2013.27568>
- Clasen, C., Eggers, J., Fontelos, M.A., Li, J., McKinley, G.H.: The beads-on-string structure of viscoelastic threads. *J. Fluid Mech.* **556**, 283–308 (2006) <https://doi.org/10.1017/S0022112006009633>
- Bazilevskii, A.V., Meyer, J.D., Rozhkov, A.N.: Dynamics and Breakup of Pulse Microjets of Polymeric Liquids. *Fluid Dyn.* **40**(3), 376–392 (2005) <https://doi.org/10.1007/s10697-005-0078-4>
- Morrison, N.F., Harlen, O.G.: Viscoelasticity in inkjet printing. *Rheol. Acta* **49**, 619–632 (2010) <https://doi.org/10.1007/S00397-009-0419-Z>
- Torres, P., Fonte, C.: Flow regimes of a single pulse of inelastic and elastic liquids from a round capillary tube. *Chem. Eng. Sci.* **248**(B) (2022) <https://doi.org/10.1016/j.ces.2021.117245>
- Turkoz, E., Perazzo, A., Kim, H., Stone, H.A., Arnold, C.B.: Impulsively Induced Jets from Viscoelastic Films for High-Resolution Printing. *Phys. Rev. Lett.* **120**, 074501 (2018) <https://doi.org/10.1103/PhysRevLett.120.074501>

- Franco-Gómez, A., Onuki, H., Yokoyama, Y., Nagatsu, Y., Tagawa, Y.: Effect of liquid elasticity on the behaviour of high-speed focused jets. *Exp. Fluids* **62**, 1–15 (2021) <https://doi.org/10.1007/s00348-020-03128-w>
- Truby, R.L., Lewis, J.A.: Printing soft matter in three dimensions. *Nature* **540**(7633), 371–378 (2016) <https://doi.org/10.1038/nature21003>
- Noor, N., Shapira, A., Edri, R., Gal, I., Wertheim, L., Dvir, T.: 3D Printing of Personalized Thick and Perfusable Cardiac Patches and Hearts. *Adv. Sci.* **6**(11), 1900344 (2019) <https://doi.org/10.1002/advs.201900344>
- Tagawa, Y., Oudalov, N., Visser, C.W., Peters, I.R., Meer, D., Sun, C., Prosperetti, A., Lohse, D.: Highly Focused Supersonic Microjets. *Phys. Rev. X* **2**, 031002 (2012) <https://doi.org/10.1103/PhysRevX.2.031002>
- Peters, I.R., Tagawa, Y., Oudalov, N., Sun, C., Prosperetti, A., Lohse, D., Meer, D.: Highly focused supersonic microjets: numerical simulations. *J. Fluid Mech.* **719**, 587–605 (2013) <https://doi.org/10.1017/jfm.2013.26>
- Gordillo, J.M., Onuki, H., Tagawa, Y.: Impulsive generation of jets by flow focusing. *J. Fluid Mech.* **894**, 3 (2020) <https://doi.org/10.1017/jfm.2020.270>
- Worthington, A.M.: *A Study of Splashes*. Longmans, Green, and Company, London (1908)
- Antkowiak, A., Brémond, N., Dizes, S.L., Villermaux, E.: Short-term dynamics of a density interface following an impact. *J. Fluid Mech.* **577**, 241–250 (2007) <https://doi.org/10.1017/S0022112007005058>
- Kiyama, A., Tagawa, Y., Ando, K., Kameda, M.: Effects of a water hammer and cavitation on jet formation in a test tube. *J. Fluid Mech.* **787**, 224–236 (2016) <https://doi.org/10.1017/jfm.2015.690>
- Onuki, H., Oi, Y., Tagawa, Y.: Microjet Generator for Highly Viscous Fluids. *Phys. Rev. Appl.* **9**, 014035 (2018) <https://doi.org/10.1103/PhysRevApplied.9.014035>
- Kiyama, A., Yuto, N., Tagawa, Y.: The generation of a liquid jet induced by a pressure impulse (experimental study on the jet velocity). *Trans. JSME (in Japanese)* **80**(814), 0151–0151 (2014) <https://doi.org/10.1299/transjsme.2014fe0151>
- Gaillard, A., Roché, M., Lerouge, S., Gay, C., Lebon, L., Limat, L.: Viscoelastic liquid curtains: experimental results on the flow of a falling sheet of polymer solution. *J. Fluid Mech.* **873**, 358–409 (2019) <https://doi.org/10.1017/jfm.2019.389>
- Dinic, J., Biagioli, M., Sharma, V.: Pinch-off dynamics and extensional relaxation times of intrinsically semi-dilute polymer solutions characterized by dripping-onto-substrate rheometry. *J. Polym. Sci. B: Polym. Phys.* **55**(22), 1692–1704 (2017)

<https://doi.org/10.1002/polb.24388>

- Dinic, J., Zhang, Y., Jimenez, L.N., Sharma, V.: Extensional Relaxation Times of Dilute, Aqueous Polymer Solutions. *ACS Macro Lett.* **4**(7), 804–808 (2015) <https://doi.org/10.1021/acsmacrolett.5b00393>
- Sur, S., Rothstein, J.: Drop breakup dynamics of dilute polymer solutions: Effect of molecular weight, concentration, and viscosity. *J. Rheol.* **62**(5), 1245–1259 (2018) <https://doi.org/10.1122/1.5038000>
- Anna, S.L., McKinley, G.H.: Elasto-capillary thinning and breakup of model elastic liquids. *J. Rheol.* **45**(1), 115–138 (2001) <https://doi.org/10.1122/1.1332389>
- Mathues, W., Formenti, S., McIlroy, C., Harlen, O.G., Clasen, C.: Caber vs ROJER—Different time scales for the thinning of a weakly elastic jet. *J. Rheol.* **62**(5), 1135–1153 (2018) <https://doi.org/10.1122/1.5021834>
- McIlroy, C., Harlen, O.G., Morrison, N.F.: Modelling the jetting of dilute polymer solutions in drop-on-demand inkjet printing. *J. Nonnewton Fluid Mech.* **201**, 17–28 (2013) <https://doi.org/10.1016/j.jnnfm.2013.05.007>
- Hoath, S.D., Harlen, O.G., Hutchings, I.M.: Jetting behavior of polymer solutions in drop-on-demand inkjet printing. *J. Rheol.* **56**(5), 1109–1127 (2012) <https://doi.org/10.1122/1.4724331>
- Turkoz, E., Stone, H.A., Arnold, C.B., Deike, L.: Simulation of impulsively induced viscoelastic jets using the oldroyd-b model. *J. Fluid Mech.* **911**, 14 (2021) <https://doi.org/10.1017/jfm.2020.1053>
- Chilcott, M.D., Rallison, J.M.: Creeping flow of dilute polymer solutions past cylinders and spheres. *J. Nonnewton Fluid Mech.* **29**, 381–432 (1988) [https://doi.org/10.1016/0377-0257\(88\)85062-6](https://doi.org/10.1016/0377-0257(88)85062-6)